Article
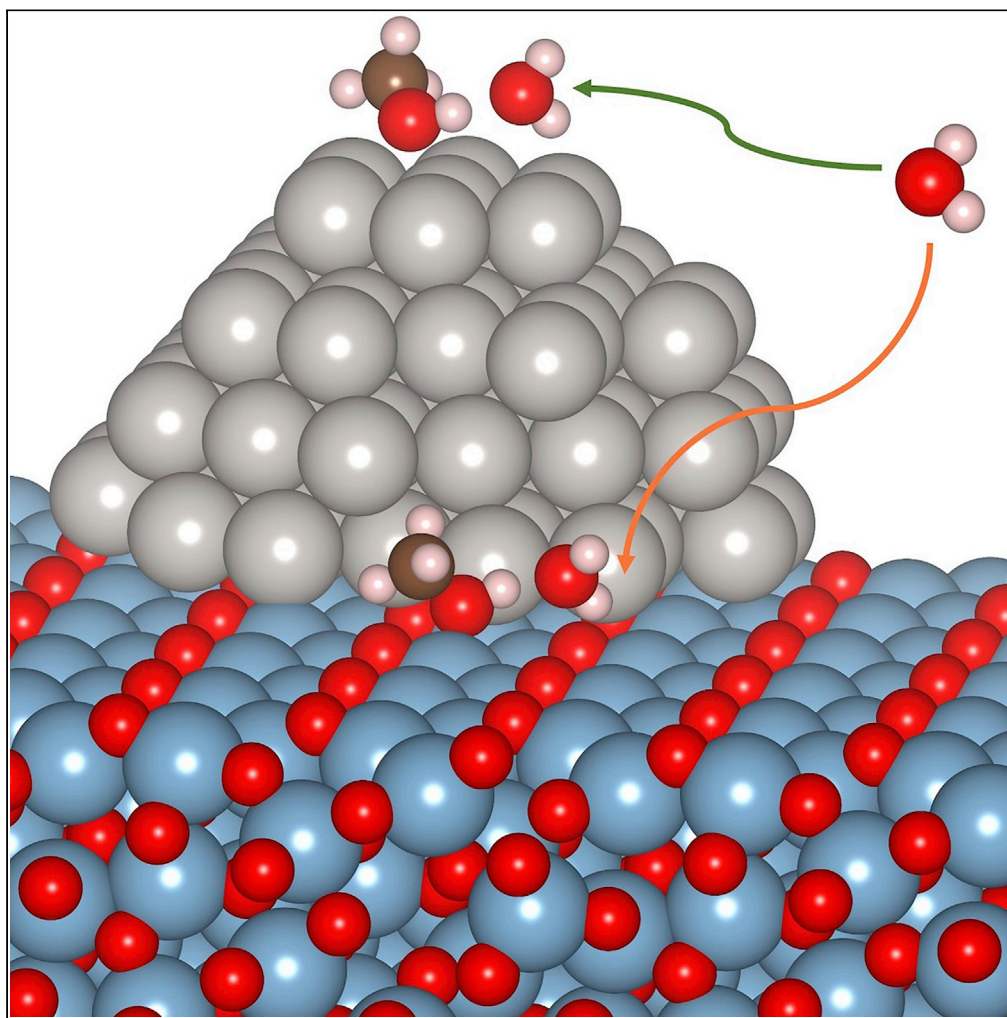
Differences in solvation thermodynamics of oxygenates at Pt/Al$_2$O$_3$ perimeter versus Pt(111) terrace sites

Ricardo A. Garcia Carcamo, Xiaohong Zhang, Ali Estejab, ..., Carsten Sievers, Sapna Sarupria, Rachel B. Getman

rgetman@clemson.edu

Highlights

Interfacial properties play an important role on adsorbate solvation thermodynamics

Pt terrace and Pt/Al$_2$O$_3$ perimeter sites exhibit entropy to energy compensation

Cavity formation also influences solvation entropy on Pt/Al$_2$O$_3$ perimeter sites

iScience

Article

Differences in solvation thermodynamics of oxygenates at Pt/Al$_2$O$_3$ perimeter versus Pt(111) terrace sites

Ricardo A. Garcia Carcamo,[1] Xiaohong Zhang,[1,4] Ali Estejab,[1,5] Jiarun Zhou,[1] Bryan J. Hare,[2] Carsten Sievers,[2,6] Sapna Sarupria,[3,6] and Rachel B. Getman[1,7,*]

SUMMARY

A prominent role of water in aqueous-phase heterogeneous catalysis is to modify free energies; however, intuition about how is based largely on pure metal surfaces or even homogeneous solutions. Using multiscale modeling with explicit liquid water molecules, we show that the influence of water on the free energies of adsorbates at metal/support interfaces is different than that on pure metal surfaces. We specifically compute free energies of solvation for methanol and its constituents on a Pt/Al$_2$O$_3$ catalyst and compare the results to analogous values calculated on a pure Pt catalyst. We find that the more hydrophilic Pt/Al$_2$O$_3$ interface leads to smaller (more positive) free energies of solvation due to an increased entropy penalty resulting from the additional work necessary to disrupt the interfacial water structure and accommodate the interfacial species. The results will be of interest in other fields, including adsorption and proteins.

INTRODUCTION

Tuning the reaction environment surrounding a catalyst active site is the heart of catalysis design, with use of solvents being a common strategy.[1] Hence, a grand challenge in catalysis research is understanding the specific ways that solvents influence catalytic chemistry.[2] For example, solvents can alter active site chemistries[3,4] and coverages,[5,6] modify reaction energetics,[7–10] stabilize intermediate species[11–13] and transition state[14] structures, promote certain reaction paths[15] and mechanisms,[16,17] and ultimately influence catalytic outcomes.[15] While significant research has been performed to elucidate these roles of solvent, intuition about how solvents will influence any particular catalytic system remains unknown. This is because solvent effects vary greatly depending on the catalytic interface.[18,19]

The dependence of interfacial properties becomes particularly important for reactions that utilize different types of active sites. An example of such a reaction is aqueous phase reforming (APR), which is a process that can produce hydrogen from derivatives of biomass under liquid water solvent.[20,21] APR is generally carried out on metal nanoparticles anchored to metal oxide supports,[20,22] and both sites on the metal components (terrace sites) and at the metal/support interface (perimeter sites) have been shown to be relevant to the observed chemistry.[23–25] However, the ways that these two types of sites promote the APR mechanism are different, even in the absence of solvent. For example, molecules tend to bind more strongly at perimeter sites than at terrace sites,[26,27] due to the presence of undercoordinated metal atoms at perimeter sites. Furthermore, metals in the support at perimeter sites can provide additional anchoring sites,[28] hence providing a richer active site environment.[29]

Solvents interact differently with these two types of sites as well. Specifically, metal sites are relatively hydrophobic,[30] whereas metal oxide supports generally comprise ions which are more attractive to solvent molecules.[31–33] The more attractive interface leads to differences in molecular and structural solvent phenomena. For example, H$_2$O molecules adsorb more strongly to more hydrophilic interfaces than to more hydrophobic interfaces, which leads to larger water densities near the interfaces of more hydrophilic surfaces.[33–35] These larger densities result in reduced mobilities for interfacial H$_2$O molecules,[36,37] which influence the free energies[38] of interfacial processes such as catalysis. Indeed, the kinetics of APR has been observed to be different at perimeter sites compared with terrace sites, with these differences being

[1]Department of Chemical and Biomolecular Engineering, Clemson University, Clemson, SC 29634, USA

[2]School of Chemical and Biomolecular Engineering, Georgia Institute of Technology, Atlanta, GA 30332, USA

[3]Department of Chemistry and Chemical Theory Center, University of Minnesota, Minneapolis, MN 55455, USA

[4]Present address: AnalyticsIQ, 6 Concourse Parkway, Suite 1750, Atlanta, GA 30328, USA

[5]Present address: Department of Chemical and Biomolecular Engineering, Lafayette College, Easton, PA 18042, USA

[6]Senior author

[7]Lead contact

*Correspondence: rgetman@clemson.edu

https://doi.org/10.1016/j.isci.2023.105980

attributed to the different roles of water in these two types of sites.[25] However, the specific ways in which water solvent influences APR at terrace versus perimeter sites remain unknown.

In this work, we begin to fill this knowledge gap by computing free energies of solvation of APR intermediates on Pt/Al_2O_3 catalysts. We chose this catalyst because it exhibits high yield and selectivity in practice.[21,22] We specifically investigate differences in solvation thermodynamics for intermediates in the pathway for methanol decomposition on Pt(111) and Pt/Al_2O_3 slabs, which serve as models for terrace and perimeter sites, respectively. Solvation thermodynamics are calculated under explicit liquid water using our previously developed method of multiscale sampling (MSS),[39] which combines density functional theory (DFT) with classical molecular dynamics (MD). The MSS method is used to compute energies (ΔE_{int}^{DFT}), entropies (ΔS_{int}^{MD}), and free energies (ΔF_{solv}^{MSS}) of solvation of CH_3OH^*, CH_2OH^*, $CHOH^*$, COH^*, CH_3O^*, CH_2O^*, CHO^*, and CO^* adsorbates (*'ed species indicate that they are adsorbed to the catalyst). Solvation thermodynamics of H^* and H_2O^* are additionally computed for completeness. We find that the strength of the water-adsorbate interaction has a strong influence on adsorbate solvation thermodynamics in terrace and perimeter sites, but solvation entropy contributes more significantly to the solvation free energy in perimeter sites due to the greater work needed to create cavities in the solvent structure at these more hydrophilic interfaces.

RESULTS

Calculated structures of adsorbates at the Pt/Al_2O_3 perimeter sites are shown in Figure 1. Additional views are provided in Table S14. With the exceptions of CO^*, COH^*, and H^*, methanol and its derivatives bind O-down to Al ions. Adsorbates with non-fully saturated methyl groups additionally bind to the Pt cluster.[28]

Calculated energies, entropies, and free energies of solvation for these adsorbates are presented in Figure 2; entropies are presented as $T\Delta S_{int}^{MD}$ to illustrate the extent to which they contribute to ΔF_{solv}^{MSS}. All adsorbates exhibit negative energies of solvation (except for H^*, which exhibits a slightly positive ΔE_{int}^{DFT} that is ~0). All adsorbates also exhibit negative entropies of solvation, in line with our prior work.[40] Free energies of solvation are positive for all adsorbates except H_2O^*, due to $T\Delta S_{int}^{MD}$ being more negative than ΔE_{int}^{DFT}. Specifically, alcohol adsorbates except for COH^* (i.e., CH_3OH^*, CH_2OH^*, and, $CHOH^*$) have $\Delta F_{solv}^{MSS} \sim 0$ due to having $T\Delta S_{int}^{MD}$ that directly compensate ΔE_{int}^{DFT}, whereas aldehyde/CO^* adsorbates except for CH_2O^* (i.e., CH_3O^*, CHO^*, and CO^*) have non-negligible ΔF_{solv}^{MSS} that are more positive than the corresponding alcohol adsorbates due to having large negative values of $T\Delta S_{int}^{MD}$. This trend of entropy of solvation compensating energy of solvation agrees with prior literature, which shows that energy and entropy of solvation are related[41–43] since the higher interaction between the solute and solvent increases the energy but at the same time restricts the motions of the solvent molecules, which leads to an entropy penalty.[42,44] Hence, entropies of solvation generally counteract energies of solvation.

Calculated solvation thermodynamics are compared with the analogous values calculated on Pt(111) in Figure 3. A color version of Figure 3 is presented in Figure S17. In general, ΔF_{solv}^{MSS} are more negative on Pt(111) than on Pt/Al_2O_3. For alcohol adsorbates with the exception of $CHOH^*$ (i.e., CH_3OH^*, CH_2OH^*, and COH^*), this is because ΔE_{int}^{DFT} on Pt(111) are large and negative and outweigh $T\Delta S_{int}^{MD}$, whereas on Pt/Al_2O_3, ΔE_{int}^{DFT} are smaller and nearly equal to $T\Delta S_{int}^{MD}$. For aldehyde/CO^* adsorbates (CH_3O^*, CH_2O^*, CHO^*, and CO^*), $T\Delta S_{int}^{MD}$ outweigh ΔE_{int}^{DFT} on Pt(111) and Pt/Al_2O_3, with the effect being more pronounced on Pt/Al_2O_3. In fact, both ΔE_{int}^{DFT} and $T\Delta S_{int}^{MD}$ are more negative for aldehyde/CO^* adsorbates on Pt/Al_2O_3 than on Pt(111).

Figure 3 shows that entropies of solvation contribute more to free energies of solvation on Pt/Al_2O_3 than on Pt(111). To explore this further, Figure 4 plots $T\Delta S_{int}^{MD}$ vs. ΔE_{int}^{DFT} for methanol decomposition intermediates on Pt/Al_2O_3 (filled black triangles) along with the analogous values for 90 C_1-C_3 oxygenate species on Pt(111) (open gray circles; taken from ref. [45]). Best fit lines are also included for both datasets. On Pt(111), the slope of $T\Delta S_{int}^{MD}$ versus ΔE_{int}^{DFT} is 0.50, which agrees with prior literature[44,46] as well as homogeneous solution theory.[47] The larger slope of 0.66 for Pt/Al_2O_3 suggests that $T\Delta S_{int}^{MD}$ contributes more significantly to ΔF_{solv}^{MSS}. Values of $T\Delta S_{int}^{MD}$ are well correlated to values of ΔE_{int}^{DFT} on Pt(111) ($R^2 = 0.91$), indicating that the energy to entropy compensation[41,44] trend is preserved on this interface (this is true even when the sample size for Pt(111) is smaller; see Figure S22). In contrast, $T\Delta S_{int}^{MD}$ are less well correlated to ΔE_{int}^{DFT} on Pt/Al_2O_3 ($R^2 = 0.62$), suggesting that other phenomena contribute to solvation enthalpies on Pt/Al_2O_3.
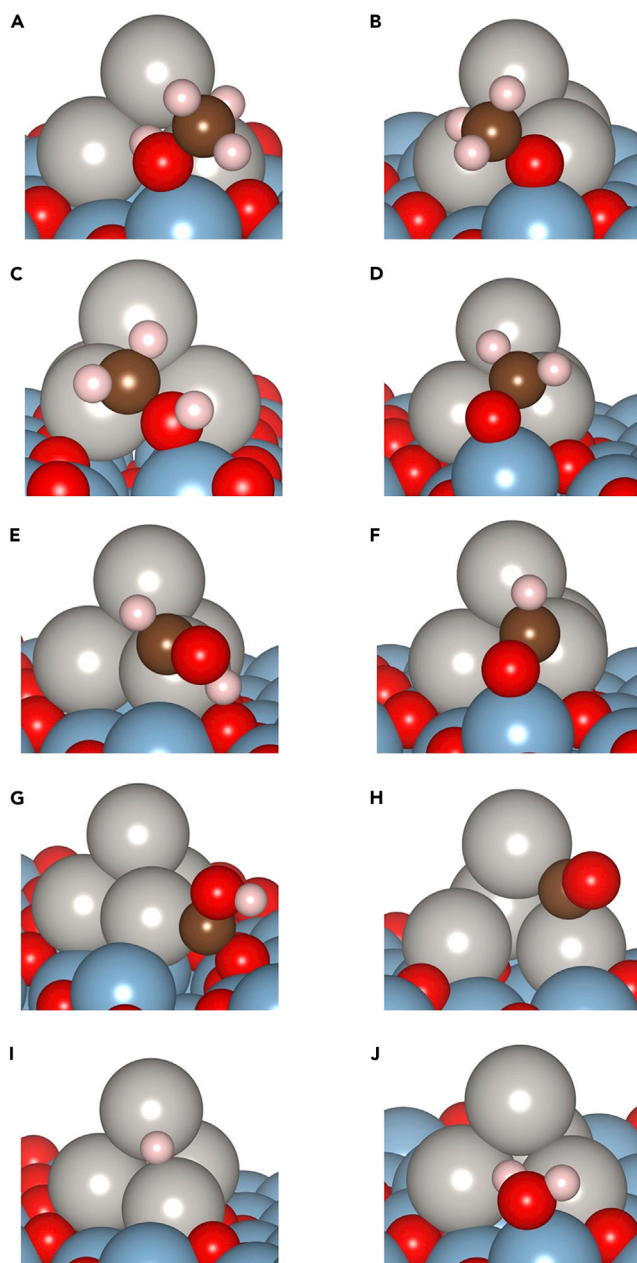
Figure 1. Calculated adsorbate geometries in Pt/Al$_2$O$_3$ perimeter sites

(A–J) (A) CH$_3$OH* (B) CH$_3$O* (C) CH$_2$OH* (D) CH$_2$O* (E) CHOH* (F) CHO* (G) COH* (H) CO* (I) H* (J) H$_2$O*. Solvent molecules are omitted for clarity. Pt = gray, Al = blue, O = red, C = brown, H = pink.

DISCUSSION

The difference in relationship between $T\Delta S_{int}^{MD}$ and ΔE_{int}^{DFT} on Pt/Al$_2$O$_3$ versus Pt(111) is caused by differences in properties for these two interfaces. Specifically, Pt(111) is less hydrophilic (exhibiting a H$_2$O molecule binding energy of −0.33 eV[48] versus −1.14 eV[49] for Al$_2$O$_3$), so solvation phenomena are largely controlled by the adsorbates themselves, resulting in the strong correlation between $T\Delta S_{int}^{MD}$ and ΔE_{int}^{DFT}. In contrast, Al$_2$O$_3$ is hydrophilic,[50] and the weaker correlation between $T\Delta S_{int}^{MD}$ and ΔE_{int}^{DFT} suggests that other phenomena in addition to the strength of the adsorbate-H$_2$O bond, particularly the H$_2$O interaction with the Al$_2$O$_3$ interface, contribute to $T\Delta S_{int}^{MD}$.
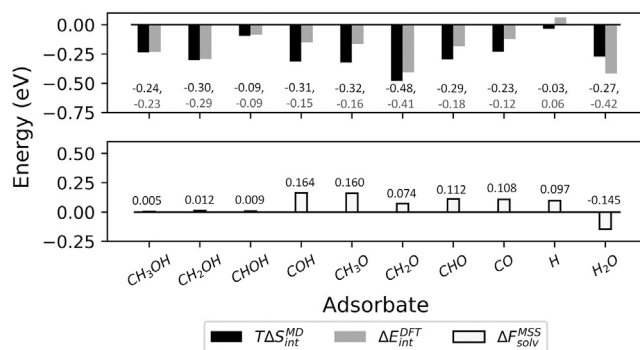
Figure 2. Calculated energies (gray bars and text), entropies (black bars and text), and free energies (white bars and black text) of solvation for methanol decomposition products on Pt/Al$_2$O$_3$ perimeter sites

To improve the understanding about solvation thermodynamics on Pt/Al$_2$O$_3$, we sought to identify the phenomena that influence $T\Delta S_{int}^{MD}$ on this interface. We showed in prior work[40] that $T\Delta S_{int}^{MD}$ on Pt(111) is related to loss of mobility/increase in "order" of H$_2$O molecules that form strong hydrogen bonds with adsorbates[40] (since hydrogen bonds hold the H$_2$O molecules in specific orientations with respect to the adsorbate and hence surface). Figure 5 shows that hydrogen bond formation either remains for the most part the same on Pt/Al$_2$O$_3$ (alcohol adsorbates except for CH$_3$OH*) or increases (aldehyde/CO* adsorbates except for CHO*) compared to Pt(111). Applying the same rationale from our prior work,[40] it is reasonable, then, that $T\Delta S_{int}^{MD}$ contributes more significantly to ΔF_{solv}^{MSS} on Pt/Al$_2$O$_3$ than on Pt(111). However, if this were the only contribution to $T\Delta S_{int}^{MD}$, we would expect better correlation between $T\Delta S_{int}^{MD}$ and ΔE_{int}^{DFT}, as on Pt(111). We hence investigated other phenomena that could contribute to $T\Delta S_{int}^{MD}$ on Pt/Al$_2$O$_3$.

We specifically investigated phenomena related to the hydrophilicity of the Al$_2$O$_3$ surface, including the H$_2$O molecule packing (see Figures S18 and S21) and solvent compressibility. The solvent compressibility was particularly insightful. The higher hydrophilicity of Al$_2$O$_3$ leads to a lower compressibility of the interfacial H$_2$O molecules (see Table S15), which means that more work is required to create a cavity in the solvent,[36,41] i.e., to accommodate adsorbates, on Pt/Al$_2$O$_3$ compared to Pt(111). One way to quantify cavity size is by the number of H$_2$O molecules that are displaced by the adsorbate. Figure 6 plots $T\Delta S_{int}^{MD}$ versus the number of displaced H$_2$O molecules for adsorbates on Pt/Al$_2$O$_3$ and Pt(111). On Pt/Al$_2$O$_3$, these two values are correlated (R^2 = 0.63), with adsorbates that exhibit larger cavities also exhibiting more negative values of $T\Delta S_{int}^{MD}$ (as with the strength of the adsorbate-H$_2$O interaction, the R^2 value of ~0.6 suggests that other phenomena in addition to cavity size contribute to $T\Delta S_{int}^{MD}$). In contrast, there is no correlation between cavity size and $T\Delta S_{int}^{MD}$ for adsorbates on Pt(111) ($R^2 \sim 0$). These results suggest that there is a higher
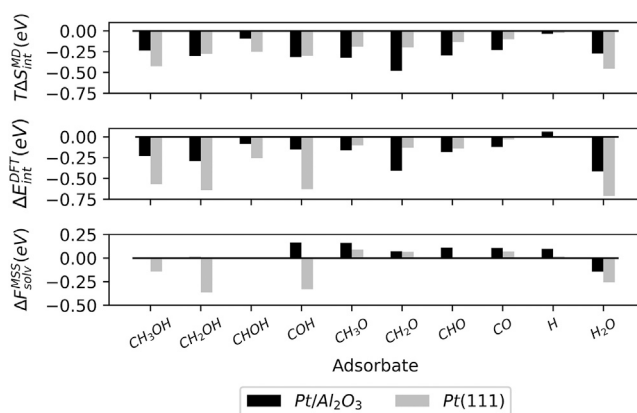
Figure 3. Comparison of solvation thermodynamics for terrace and perimeter sites
Calculated entropies (top), energies (middle), and free energies (bottom) of solvation for methanol decomposition products on Pt/Al$_2$O$_3$ perimeter sites (black) versus Pt(111) terrace sites (gray).
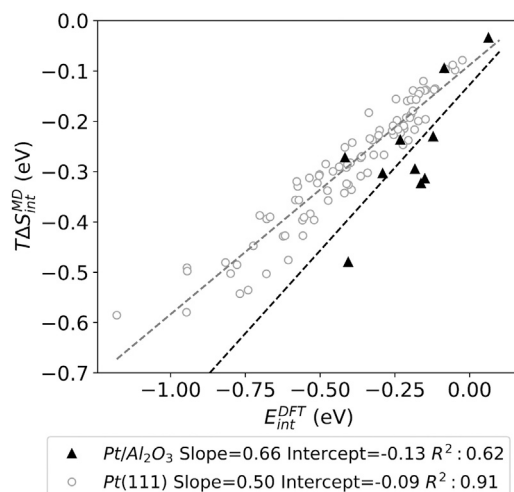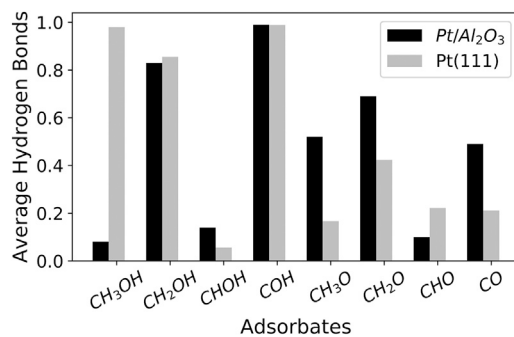
Figure 4. $T\Delta S_{int}^{MD}$ plotted against ΔE_{int}^{DFT} for adsorbates in Pt/Al$_2$O$_3$ perimeter sites (filled black triangles) and Pt(111) terrace (open gray circles)

entropy penalty associated with cavity formation[38,51] on Pt/Al$_2$O$_3$ than on Pt(111). This entropy penalty decreases (makes more negative) the entropies of solvation on Pt/Al$_2$O$_3$. Furthermore, since this effect is related more to the water-surface interaction rather than the water-adsorbate interaction (ΔE_{int}^{DFT}), it detracts from the correlation between ΔE_{int}^{DFT} and $T\Delta S_{int}^{MD}$, resulting in a lower R^2 value than on Pt(111). In other words, the strength of the water-adsorbate interaction determines the entropy of solvation on Pt(111), whereas both the strength of the water-adsorbate interaction and the cavity size determine the entropy of solvation on Pt/Al$_2$O$_3$.

These findings suggest that solvation thermodynamics on the terrace versus perimeter sites on Pt catalysts supported on Al$_2$O$_3$ are different. Specifically, while the solvation thermodynamics in Pt terrace sites depend almost entirely on the adsorbate and the strength of the hydrogen bonds that it forms with liquid H$_2$O molecules, interfacial properties have a strong influence on solvation thermodynamics of adsorbates in Pt/Al$_2$O$_3$ perimeter sites due to the higher interfacial hydrophilicity. This study illustrates how interfacial properties influence solvation thermodynamics of adsorbed species and the significant role that entropy can play in the solvation thermodynamics of adsorbed species. The insight provided herein will help expand intuition about solvation thermodynamics of interfacial species, which will be helpful in catalysis and other fields.

Limitations of the study

The accuracies of the calculated values depend on the intrinsic accuracies of the methods used to compute system energies, including DFT as well as the force fields employed in the MD simulations. These topics are

Figure 5. Comparison of hydrogen bond formation for adsorbates in Pt/Al$_2$O$_3$ perimeter sites (black bars) and Pt(111) terrace sites (gray bars)
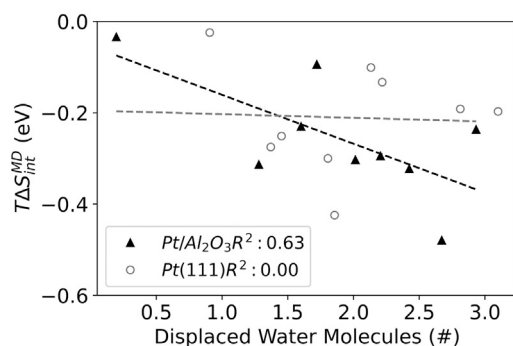
Figure 6. $T\Delta S_{int}^{MD}$ **versus number of displaced H$_2$O molecules for adsorbates in Pt/Al$_2$O$_3$ perimeter sites (filled black triangles) and Pt(111) terrace sites (open gray circles)**

discussed in detail in the STAR Methods (see the model validation sections). Furthermore, the exact values of the energies are illustrative of the specific model systems employed (the interested reader can find simple correlations that can be used to estimate these values in Figures S19 and S20). Not only are these model systems likely simpler than real catalyst systems (with simplifications made for reasons of computational tractability) but real catalyst interfaces also likely exhibit distributions of active sites, with multiple active sites within the distribution contributing to the observed solvation thermodynamics. None of these limitations should influence the overall conclusions presented above. Furthermore, under reaction conditions, active sites will likely comprise finite coverages of adsorbates, whereas the active sites herein were modeled at low coverage. In some circumstances, coverage effects could influence interfacial properties and hence the calculated solvation thermodynamics. The potential influence of coverage on interfacial properties and solvation thermodynamics should be considered on a case-by-case basis. Finally, this study only investigates solvation thermodynamics, while the influences of solvation on adsorption, desorption, and the reaction mechanism are reserved for future work. The influence of temperature on the solvation thermodynamics is also reserved for future work.

STAR★METHODS

Detailed methods are provided in the online version of this paper and include the following:

- KEY RESOURCES TABLE
- RESOURCE AVAILABILITY
  - Lead contact
  - Materials availability
  - Data and code availability
- METHOD DETAILS
  - Pt/Al$_2$O$_3$ simulation supercells
  - Solvation free energies
  - Classical molecular dynamics simulations for Pt/Al$_2$O$_3$ systems
  - DFT calculations
  - Model validation: Simulation supercells for the perimeter sites
  - Model validation: Density profiles for the perimeter sites
  - Pt(111) simulation supercells
  - Classic molecular dynamics simulations for Pt(111) systems
  - List of adsorbates included used for solvation thermodynamic trend for terrace sites
  - Model validation: Effect of calculated partial charges on solvation entropy for the Pt/Al$_2$O$_3$ systems
  - Model validation: Testing of the platinum particle size on the solvation entropy for the Pt/Al$_2$O$_3$ systems
  - Model validation: Testing of the platinum particle size for interaction energy with DFT
  - Model validation: Testing for the solvation thermodynamics for the slab size in the terrace site Pt(111) model
  - Model validation: Selection of the water model
  - Lennard-Jones and Coulomb parameters used in the MD simulations for Pt/Al$_2$O$_3$ systems
  - Rationale for modifying the Lennard-Jones epsilon parameter for Pt atoms in the Pt/Al$_2$O$_3$ systems

- ○ Development of Coulomb charges for MD simulations from DFT calculated partial charges for the Pt/Al$_2$O$_3$ systems
- ○ Reflective wall in MD simulations for Pt/Al$_2$O$_3$ systems
- ○ Justification of scaling strategy used for the FEP simulations of the Pt/Al$_2$O$_3$ systems
- ○ Comparison of free energy between the multiscale sampling method and implicit solvation
- ○ Order parameters for water structure
- ○ Isothermal compressibility of water
- ○ Effect of the sample size in the coefficient of determination for the entropy and interaction energies in Pt(111)

AUTHOR CONTRIBUTIONS

R.A.G.C., conceptualization, methodology, validation, formal analysis, investigation, writing the original draft, reviewing, and editing; X.Z., methodology, investigation, and writing – review & editing; A.E., methodology and writing – review & editing; J.Z., methodology and writing – review & editing; B.J.H., conceptualization and writing – review & editing; C.S., conceptualization, writing – review & editing, supervision, and funding acquisition; S.S., methodology, writing – review & editing, and supervision; R.B.G., conceptualization, methodology, resources, writing – review & editing, supervision, project administration, and funding acquisition.

DECLARATION OF INTERESTS

The authors declare no competing interests.

INCLUSION AND DIVERSITY

We support inclusive, diverse, and equitable conduct of research.

REFERENCES

1. Li, G., Wang, B., and Resasco, D.E. (2021). Solvent effects on catalytic reactions and related phenomena at liquid-solid interfaces. Surf. Sci. Rep. 76, 100541. https://doi.org/10.1016/j.surfrep.2021.100541.

2. Dai, Y., Li, G., Resasco, D.E., and Yang, Y. (2021). How do structure and topology of the catalyst affect water promotion or inhibition effects? Chem Catalysis 1, 962–965. https://doi.org/10.1016/j.checat.2021.09.006.

3. Jenness, G.R., Christiansen, M.A., Caratzoulas, S., Vlachos, D.G., and Gorte, R.J. (2014). Site-Dependent lewis acidity of γ-Al2O3 and its impact on ethanol dehydration and etherification. J. Phys. Chem. C 118, 12899–12907. https://doi.org/10.1021/jp5028349.

4. Santos, K.M.A., Albuquerque, E.M., Innocenti, G., Borges, L.E.P., Sievers, C., and Fraga, M.A. (2019). The role of brønsted and water-tolerant lewis acid sites in the cascade aqueous-phase reaction of triose to lactic acid. ChemCatChem 11, 3054–3063. https://doi.org/10.1002/cctc.201900519.

5. Steinmann, S.N., and Michel, C. (2022). How to gain atomistic insights on reactions at the water/solid interface? ACS Catal. 12, 6294–6301. https://doi.org/10.1021/acscatal.2c00594.

6. Montemore, M.M., Andreussi, O., and Medlin, J.W. (2016). Hydrocarbon adsorption in an aqueous environment: a computational study of alkyls on Cu(111). J. Chem. Phys. 145, 074702. https://doi.org/10.1063/1.4961027.

7. Faheem, M., Suthirakun, S., and Heyden, A. (2012). New implicit solvation scheme for solid surfaces. J. Phys. Chem. C 116, 22458–22462. https://doi.org/10.1021/jp308212h.

8. Saleheen, M., Zare, M., Faheem, M., and Heyden, A. (2019). Computational investigation of aqueous phase effects on the dehydrogenation and dehydroxylation of polyols over Pt(111). J. Phys. Chem. C 123, 19052–19065. https://doi.org/10.1021/acs.jpcc.9b04994.

9. Faheem, M., and Heyden, A. (2014). Hybrid quantum mechanics/molecular mechanics solvation scheme for computing free energies of reactions at metal–water interfaces. J. Chem. Theor. Comput. 10, 3354–3368. https://doi.org/10.1021/ct500211w.

10. Ruiz-Lopez, M.F., Francisco, J.S., Martins-Costa, M.T.C., and Anglada, J.M. (2020). Molecular reactions at aqueous interfaces. Nat. Rev. Chem 4, 459–475. https://doi.org/10.1038/s41570-020-0203-2.

11. Mei, Y., and Deskins, N.A. (2021). An evaluation of solvent effects and ethanol oxidation. Phys. Chem. Chem. Phys. 23, 16180–16192. https://doi.org/10.1039/D1CP00630D.

12. Steinmann, S.N., Sautet, P., and Michel, C. (2016). Solvation free energies for periodic surfaces: comparison of implicit and explicit solvation models. Phys. Chem. Chem. Phys. 18, 31850–31861. https://doi.org/10.1039/C6CP04094B.

13. Clabaut, P., Schweitzer, B., Götz, A.W., Michel, C., and Steinmann, S.N. (2020). Solvation free energies and adsorption energies at the metal/water interface from hybrid quantum-mechanical/molecular mechanics simulations. J. Chem. Theor. Comput. 16, 6539–6549. https://doi.org/10.1021/acs.jctc.0c00632.

14. Bodenschatz, C.J., Xie, T., Zhang, X., and Getman, R.B. (2019). Insights into how the aqueous environment influences the kinetics and mechanisms of heterogeneously-catalyzed COH and CH3OH dehydrogenation reactions on Pt(111). Phys. Chem. Chem. Phys. 21, 9895–9904. https://doi.org/10.1039/C9CP00824A.

15. Gu, G.H., Wittreich, G.R., and Vlachos, D.G. (2019). Microkinetic modeling of aqueous phase biomass conversion: application to ethylene glycol reforming. Chem. Eng. Sci. 197, 415–418. https://doi.org/10.1016/j.ces.2018.12.036.

16. Ripken, R.M., Meuldijk, J., Gardeniers, J.G.E., and Le Gac, S. (2017). Influence of the water phase state on the thermodynamics of aqueous-phase reforming for hydrogen production. ChemSusChem 10, 4909–4913. https://doi.org/10.1002/cssc.201700189.

17. Seretis, A., and Tsiakaras, P. (2015). A thermodynamic analysis of hydrogen production via aqueous phase reforming of glycerol. Fuel Process. Technol. 134, 107–115. https://doi.org/10.1016/j.fuproc.2015.01.021.

18. Cordon, M.J., Harris, J.W., Vega-Vila, J.C., Bates, J.S., Kaur, S., Gupta, M., Witzke, M.E., Wegener, E.C., Miller, J.T., Flaherty, D.W., et al. (2018). Dominant role of entropy in stabilizing sugar isomerization transition states within hydrophobic zeolite pores. J. Am. Chem. Soc. 140, 14244–14266. https://doi.org/10.1021/jacs.8b08336.

19. Antony, A.C., Liang, T., Akhade, S.A., Janik, M.J., Phillpot, S.R., and Sinnott, S.B. (2016). Effect of surface chemistry on water interaction with Cu(111). Langmuir 32, 8061–8070. https://doi.org/10.1021/acs.langmuir.6b01974.

20. Davda, R.R., Shabaker, J.W., Huber, G.W., Cortright, R.D., and Dumesic, J.A. (2005). A review of catalytic issues and process conditions for renewable hydrogen and alkanes by aqueous-phase reforming of oxygenated hydrocarbons over supported metal catalysts. Appl. Catal. B Environ. 56, 171–186. https://doi.org/10.1016/j.apcatb.2004.04.027.

21. Coronado, I., Stekrova, M., Reinikainen, M., Simell, P., Lefferts, L., and Lehtonen, J. (2016). A review of catalytic aqueous-phase reforming of oxygenated hydrocarbons derived from biorefinery water fractions. Int. J. Hydrogen Energy 41, 11003–11032. https://doi.org/10.1016/j.ijhydene.2016.05.032.

22. Ciftci, A., Peng, B., Jentys, A., Lercher, J.A., and Hensen, E.J.M. (2012). Support effects in the aqueous phase reforming of glycerol over supported platinum catalysts. Appl. Catal. Gen. 431–432, 113–119. https://doi.org/10.1016/j.apcata.2012.04.026.

23. Ammal, S.C., and Heyden, A. (2011). Nature of ptn/TiO2(110) interface under water-gas shift reaction conditions: a constrained ab initio thermodynamics study. J. Phys. Chem. C 115, 19246–19259. https://doi.org/10.1021/jp2058723.

24. Walker, E.A., Mitchell, D., Terejanu, G.A., and Heyden, A. (2018). Identifying active sites of the water–gas shift reaction over titania supported platinum catalysts under uncertainty. ACS Catal. 8, 3990–3998. https://doi.org/10.1021/acscatal.7b03531.

25. Hare, B.J., Garcia Carcamo, R.A., Xie, T., Meza-Morales, P.J., Getman, R.B., and Sievers, C. (2021). Active sites and effects of co-adsorbed H2O on isolated methanol dehydrogenation over Pt/γ-Al2O3. J. Catal. 402, 218–228. https://doi.org/10.1016/j.jcat.2021.08.027.

26. Halder, A., Ha, M.-A., Zhai, H., Yang, B., Pellin, M.J., Seifert, S., Alexandrova, A.N., and Vajda, S. (2020). Oxidative dehydrogenation of cyclohexane by Cu vs Pd clusters: selectivity control by specific cluster dynamics. ChemCatChem 12, 1307–1315. https://doi.org/10.1002/cctc.201901795.

27. Zhao, Z.-J., Li, Z., Cui, Y., Zhu, H., Schneider, W.F., Delgass, W.N., Ribeiro, F., and Greeley, J. (2017). Importance of metal-oxide interfaces in heterogeneous catalysis: a combined DFT, microkinetic, and experimental study of water-gas shift on Au/MgO. J. Catal. 345, 157–169. https://doi.org/10.1016/j.jcat.2016.11.008.

28. Xie, T., Hare, B.J., Meza-Morales, P.J., Sievers, C., and Getman, R.B. (2020). Identification of the active sites in the dehydrogenation of methanol on Pt/Al2O3 catalysts. J. Phys. Chem. C 124, 19015–19023. https://doi.org/10.1021/acs.jpcc.0c03717.

29. Liu, B., Liu, J., Li, T., Zhao, Z., Gong, X.-Q., Chen, Y., Duan, A., Jiang, G., and Wei, Y. (2015). Interfacial effects of CeO2-supported Pd nanorod in catalytic CO oxidation: a theoretical study. J. Phys. Chem. C 119, 12923–12934. https://doi.org/10.1021/acs.jpcc.5b00267.

30. Limmer, D.T., Willard, A.P., Madden, P., and Chandler, D. (2013). Hydration of metal surfaces can be dynamically heterogeneous and hydrophobic. Proc. Natl. Acad. Sci. USA 110, 4200–4205. https://doi.org/10.1073/pnas.1301596110.

31. Mavrič, A., Valant, M., Cui, C., and Wang, Z.M. (2019). Advanced applications of amorphous alumina: from nano to bulk. J. Non-Cryst. Solids 521, 119493. https://doi.org/10.1016/j.jnoncrysol.2019.119493.

32. Saien, J., Moghaddamnia, F., and Bamdadi, H. (2013). Interfacial tension of methylbenzene–water in the presence of hydrophilic and hydrophobic alumina nanoparticles at different temperatures. J. Chem. Eng. Data 58, 436–440. https://doi.org/10.1021/je3011584.

33. Argyris, D., Ho, T., Cole, D.R., and Striolo, A. (2011). Molecular dynamics studies of interfacial water at the alumina surface. J. Phys. Chem. C 115, 2038–2046. https://doi.org/10.1021/jp109244c.

34. Harmon, K.J., Chen, Y., Bylaska, E.J., Catalano, J.G., Bedzyk, M.J., Weare, J.H., and Fenter, P. (2018). Insights on the alumina–water interface structure by direct comparison of density functional simulations with X-ray reflectivity. J. Phys. Chem. C 122, 26934–26944. https://doi.org/10.1021/acs.jpcc.8b08522.

35. Petrik, N.G., Huestis, P.L., LaVerne, J.A., Aleksandrov, A.B., Orlando, T.M., and Kimmel, G.A. (2018). Molecular water adsorption and reactions on α-Al2O3(0001) and α-alumina particles. J. Phys. Chem. C 122, 9540–9551. https://doi.org/10.1021/acs.jpcc.8b01969.

36. Godawat, R., Jamadagni, S.N., and Garde, S. (2009). Characterizing hydrophobicity of interfaces by using cavity formation, solute binding, and water correlations. Proc. Natl. Acad. Sci. USA 106, 15119–15124. https://doi.org/10.1073/pnas.0902778106.

37. Ho, T.A., Papavassiliou, D.V., Lee, L.L., and Striolo, A. (2011). Liquid water can slip on a hydrophilic surface. Proc. Natl. Acad. Sci. USA 108, 16170–16175. https://doi.org/10.1073/pnas.1105189108.

38. Liu, M., Besford, Q.A., Mulvaney, T., and Gray-Weale, A. (2015). Order and correlation contributions to the entropy of hydrophobic solvation. J. Chem. Phys. 142, 114117. https://doi.org/10.1063/1.4908532.

39. Bodenschatz, C.J., Zhang, X., Xie, T., Arvay, J., Sarupria, S., and Getman, R.B. (2019). Multiscale sampling of a heterogeneous water/metal catalyst interface using density functional theory and force-field molecular dynamics. JoVE 146, e59284. https://doi.org/10.3791/59284.

40. Zhang, X., DeFever, R.S., Sarupria, S., and Getman, R.B. (2019). Free energies of catalytic species adsorbed to Pt(111) surfaces under liquid solvent calculated using classical and quantum approaches. J. Chem. Inf. Model. 59, 2190–2198. https://doi.org/10.1021/acs.jcim.9b00089.

41. Ben-Naim, A. (2009). Molecular theory of water and aqueous solutions. In Anonymous (World Scientific Publishing Company), p. 660. https://doi.org/10.1142/7136.

42. Sedlmeier, F., Horinek, D., and Netz, R.R. (2011). Entropy and enthalpy convergence of hydrophobic solvation beyond the hard-sphere limit. J. Chem. Phys. 134, 055105. https://doi.org/10.1063/1.3530585.

43. Leung, D.H., Bergman, R.G., and Raymond, K.N. (2008). Enthalpy−Entropy compensation reveals solvent reorganization as a driving force for supramolecular encapsulation in water. J. Am. Chem. Soc. 130, 2798–2805. https://doi.org/10.1021/ja075975z.

44. Dragan, A.I., Read, C.M., and Crane-Robinson, C. (2017). Enthalpy-entropy compensation: the role of solvation. Eur. Biophys. J. 46, 301–308. https://doi.org/10.1007/s00249-016-1182-6.

45. Zhang, X. (2021). Development of Improved Models for Simulating Adsorption Kinetics and Solvation Free Energies of Catalytic Species at Pt(111)/Liquid Water Interfaces. ProQuest Dissertations and Theses. http://libproxy.clemson.edu/login?url=https://www.proquest.com/dissertations-theses/development-improved-models-simulating-adsorption/docview/2576922001/se-2?accountid=6167.

46. Saleheen, M., and Heyden, A. (2018). Liquid-phase modeling in heterogeneous catalysis. ACS Catal. 8, 2188–2194. https://doi.org/10.1021/acscatal.7b04367.

47. Israelachvili, J.N. (2010). Intermolecular and Surface Forces. In Anonymous, Third ed. (Elsevier Science & Technology). https://doi.org/10.1016/C2009-0-21560-1.

48. Phatak, A.A., Delgass, W.N., Ribeiro, F.H., and Schneider, W.F. (2009). Density functional theory comparison of water dissociation steps on Cu, Au, Ni, Pd, and Pt. J. Phys. Chem. C 113, 7269–7276. https://doi.org/10.1021/jp810216b.

49. Ranea, V.A., Schneider, W.F., and Carmichael, I. (2008). DFT characterization of coverage dependent molecular water adsorption modes on α-Al2O3(0001). Surf. Sci. 602, 268–275. https://doi.org/10.1016/j.susc.2007.10.029.

50. Wirth, J., and Saalfrank, P. (2012). The chemistry of water on α-alumina: kinetics and nuclear quantum effects from first principles. J. Phys. Chem. C 116, 26829–26840. https://doi.org/10.1021/jp310234h.

51. Garza, A.J. (2019). Solvation entropy made simple. J. Chem. Theor. Comput. 15, 3204–3214. https://doi.org/10.1021/acs.jctc.9b00214.

52. Rey, J., Clabaut, P., Réocreux, R., Steinmann, S.N., and Michel, C. (2022). Mechanistic investigation and free energies of the reactive adsorption of ethanol at the alumina/water interface. https://doi.org/10.26434/CHEMRXIV-2021-N77JN-V2.

53. Jain, A., Ong, S.P., Hautier, G., Chen, W., Richards, W.D., Dacek, S., Cholia, S., Gunter, D., Skinner, D., Ceder, G., and Persson, K.A. (2013). The Materials Project: a materials genome approach to accelerating materials innovation. Apl. Mater. 1, 011002. https://doi.org/10.1063/1.4812323.

54. Estejab, A., García Cárcamo, R.A., and Getman, R.B. (2022). Influence of an electrified interface on the entropy and energy of solvation of methanol oxidation intermediates on platinum (111) under explicit solvation. Phys. Chem. Chem. Phys. 24, 4251–4261.

55. Bodenschatz, C.J., Sarupria, S., and Getman, R.B. (2015). Molecular-level details about liquid H2O interactions with CO and sugar alcohol adsorbates on Pt(111) calculated using density functional theory and molecular dynamics. J. Phys. Chem. C 119, 13642–13651. https://doi.org/10.1021/acs.jpcc.5b02333.

56. Zhang, X., Savara, A., and Getman, R.B. (2020). A method for obtaining liquid–solid adsorption rates from molecular dynamics simulations: applied to methanol on Pt(111) in H2O. J. Chem. Theor. Comput. 16, 2680–2691. https://doi.org/10.1021/acs.jctc.9b01249.

57. Rice, P.S., Mao, Y., Guo, C., and Hu, P. (2019). Interconversion of hydrated protons at the interface between liquid water and platinum. Phys. Chem. Chem. Phys. 21, 5932–5940. https://doi.org/10.1039/C8CP07511E.

58. Xie, T., Bodenschatz, C.J., and Getman, R.B. (2019). Insights into the roles of water on the aqueous phase reforming of glycerol. React. Chem. Eng. 4, 383–392. https://doi.org/10.1039/C8RE00267C.

59. Plimpton, S. (1995). Fast parallel algorithms for short-range molecular dynamics. J. Comput. Phys. 117, 1–19. https://doi.org/10.1006/jcph.1995.1039.

60. Nosé, S. (1984). A molecular dynamics method for simulations in the canonical ensemble. Mol. Phys. 52, 255–268. https://doi.org/10.1080/00268978400101201.

61. Hoover, W. (1985). Canonical dynamics: equilibrium phase-space distributions. Phys. Rev. A Gen. Phys. 31, 1695–1697. https://doi.org/10.1103/PhysRevA.31.1695.

62. Luzar, A., and Chandler, D. (1996). Hydrogen-bond kinetics in liquid water. Nature 379, 55–57. https://doi.org/10.1038/379055a0.

63. Buneman, O. (1983). Computer simulation using particles. SIAM Rev. Soc. Ind. Appl. Math. 25, 425–426. https://doi.org/10.1137/1025102.

64. Damm, W., Frontera, A., Tirado-Rives, J., and Jorgensen, W.L. (1997). OPLS all-atom force field for carbohydrates. J. Comput. Chem. 18, 1955–1970. https://doi.org/10.1002/(SICI)1096-987X(199712)18:163.0.CO;2-L.

65. Rappe, A.K., Casewit, C.J., Colwell, K.S., Goddard, W.A., and Skiff, W.M. (1992). UFF, a full periodic table force field for molecular mechanics and molecular dynamics simulations. J. Am. Chem. Soc. 114, 10024–10035. https://doi.org/10.1021/ja00051a040.

66. Lid, S., Köppen, S., and Colombi Ciacchi, L. (2017). Creation of models and parametrization of a classical force field for amorphous Al2O3/water interfaces based on Density Functional Theory. Comput. Mater. Sci. 140, 307–314. https://doi.org/10.1016/j.commatsci.2017.09.003.

67. MacKerell, A.D., Bashford, D., Bellott, M., Dunbrack, R.L., Evanseck, J.D., Field, M.J., Fischer, S., Gao, J., Guo, H., Ha, S., et al. (1998). All-atom empirical potential for molecular modeling and dynamics studies of proteins. J. Phys. Chem. B 102, 3586–3616. https://doi.org/10.1021/jp973084f.

68. Shivakumar, D., Williams, J., Wu, Y., Damm, W., Shelley, J., and Sherman, W. (2010). Prediction of absolute solvation free energies using molecular dynamics free energy perturbation and the OPLS force field. J. Chem. Theor. Comput. 6, 1509–1519. https://doi.org/10.1021/ct900587b.

69. Hess, B., van der Vegt, N.F.A., and Nico, F.A. (2006). Hydration thermodynamic properties of amino acid analogues: a systematic comparison of biomolecular force fields and water models. J. Phys. Chem. B 110, 17616–17626. https://doi.org/10.1021/jp0641029.

70. Berendsen, H.J.C., Grigera, J.R., and Straatsma, T.P. (1987). The missing term in effective pair potentials. J. Phys. Chem. A 91, 6269–6271.

71. Limas, N.G., and Manz, T.A. (2018). Introducing DDEC6 atomic population analysis: part 4. Efficient parallel computation of net atomic charges, atomic spin moments, bond orders, and more. RSC Adv. 8, 2678–2707. https://doi.org/10.1039/C7RA11829E.

72. Tuckerman, M.E. (2007). Free Energy Calculations: Theory and Applications in Chemistry and Biology Springer Series in Chemical Physics, 86 Edited by Christophe Chipot (Université Henri Poincaré Vandoeuvre-lès-Nancy, France) and Andrew Pohorille (University of California, San Francisco, USA). Springer: Berlin, Heidelberg, New York. 2007. xviii + 518 pp. ISBN 978-3-540-38447-2. J. Am. Chem. Soc. 129, 10963–10964. https://doi.org/10.1021/ja076952n.

73. Leach, A.R. (2001). In Molecular modelling: principles and applications, 2nd Edition (New York: Prentice Hall).

74. Pohorille, A., Jarzynski, C., and Chipot, C. (2010). Good practices in free-energy calculations. J. Phys. Chem. B 114, 10235–10253. https://doi.org/10.1021/jp102971x.

75. Hansen, N., and van Gunsteren, W.F. (2014). Practical aspects of free-energy calculations: a review. J. Chem. Theor. Comput. 10, 2632–2647. https://doi.org/10.1021/ct500161f.

76. Kresse, G., and Hafner, J. (1993). Ab initio molecular dynamics for liquid metals. Phys. Rev. B Condens. Matter *47*, 558–561. https://doi.org/10.1103/PhysRevB.47.558.

77. Kresse, G., and Furthmüller, J. (1996). Efficiency of ab-initio total energy calculations for metals and semiconductors using a plane-wave basis set. Comput. Mater. Sci. *6*, 15–50. https://doi.org/10.1016/0927-0256(96)00008-0.

78. Kresse, G., and Furthmüller, J. (1996). Efficient iterative schemes for ab initio total-energy calculations using a plane-wave basis set. Phys. Rev. B Condens. Matter *54*, 11169–11186. https://doi.org/10.1103/PhysRevB.54.11169.

79. Hacene, M., Anciaux-Sedrakian, A., Rozanska, X., Klahr, D., Guignon, T., and Fleurat-Lessard, P. (2012). Accelerating VASP electronic structure calculations using graphic processing units. J. Comput. Chem. *33*, 2581–2589. https://doi.org/10.1002/jcc.23096.

80. Hutchinson, M., and Widom, M. (2012). VASP on a GPU: application to exact-exchange calculations of the stability of elemental boron. Comput. Phys. Commun. *183*, 1422–1426. https://doi.org/10.1016/j.cpc.2012.02.017.

81. Mortensen, J.J., Hansen, L.B., and Jacobsen, K.W. (2005). Real-space grid implementation of the projector augmented wave method. Phys. Rev. B *71*, 035109. https://doi.org/10.1103/physrevb.71.035109.

82. Kresse, G., and Joubert, D. (1999). From ultrasoft pseudopotentials to the projector augmented-wave method. Phys. Rev. B *59*, 1758–1775. https://doi.org/10.1103/PhysRevB.59.1758.

83. Perdew, J., Burke, K., and Ernzerhof, M. (1996). Generalized gradient approximation made simple. Phys. Rev. Lett. *77*, 3865–3868. https://doi.org/10.1103/PhysRevLett.77.3865.

84. Perdew, J.P., Burke, K., and Ernzerhof, M. (1997). Generalized gradient approximation made simple [phys. Rev. Lett. 77, 3865 (1996)]. Phys. Rev. Lett. *78*, 1396. https://doi.org/10.1103/PhysRevLett.78.1396.

85. Grimme, S., Antony, J., Ehrlich, S., and Krieg, H. (2010). A consistent and accurate ab initio parametrization of density functional dispersion correction (DFT-D) for the 94 elements H-Pu. J. Chem. Phys. *132*, 154104. https://doi.org/10.1063/1.3382344.

86. Grimme, S., Ehrlich, S., and Goerigk, L. (2011). Effect of the damping function in dispersion corrected density functional theory. J. Comput. Chem. *32*, 1456–1465. https://doi.org/10.1002/jcc.21759.

87. Monkhorst, H.J., and Pack, J.D. (1976). Special points for Brillouin-zone integrations. Phys. Rev. B *13*, 5188–5192. https://doi.org/10.1103/PhysRevB.13.5188.

88. Lee, S.H., and Rossky, P.J. (1994). A comparison of the structure and dynamics of liquid water at hydrophobic and hydrophilic surfaces—a molecular dynamics simulation study. J. Chem. Phys. *100*, 3334–3345. https://doi.org/10.1063/1.466425.

89. Li, Q., García-Muelas, R., and López, N. (2018). Microkinetics of alcohol reforming for H2 production from a FAIR density functional theory database. Nat. Commun. *9*, 526. https://doi.org/10.1038/s41467-018-02884-y.

90. Zhang, X., and Ricardo, G.-C. (2022). Getman Research Group – Structure repository for solvation thermodynamics in Pt(111). https://github.com/getman-research-group/Structure-repository-for-solvation-thermodynamics-in-Pt-111-.

91. Izadi, S., Anandakrishnan, R., and Onufriev, A.V. (2014). Building water models: a different approach. J. Phys. Chem. Lett. *5*, 3863–3871. https://doi.org/10.1021/jz501780a.

92. Jorgensen, W.L., Chandrasekhar, J., Madura, J.D., Impey, R.W., and Klein, M.L. (1983). Comparison of simple potential functions for simulating liquid water. J. Chem. Phys. *79*, 926–935. https://doi.org/10.1063/1.445869.

93. Heinz, H., Vaia, R.A., Farmer, B.L., and Naik, R.R. (2008). Accurate simulation of surfaces and interfaces of face-centered cubic metals using 12−6 and 9−6 Lennard-Jones potentials. J. Phys. Chem. C *112*, 17281–17290. https://doi.org/10.1021/jp801931d.

94. Mager-Maury, C., Chizallet, C., Sautet, P., and Raybaud, P. (2012). Platinum nanoclusters stabilized on γ-alumina by chlorine used as a capping surface ligand: a density functional theory study. ACS Catal. *2*, 1346–1357. https://doi.org/10.1021/cs300178y.

95. Johansson, P., and Hess, B. (2018). Molecular origin of contact line friction in dynamic wetting. Phys. Rev. Fluids *3*, 074201. https://doi.org/10.1103/PhysRevFluids.3.074201.

96. Mathew, K., Sundararaman, R., Letchworth-Weaver, K., Arias, T.A., and Hennig, R.G. (2014). Implicit solvation model for density-functional study of nanocrystal surfaces and reaction pathways. J. Chem. Phys. *140*, 084106. https://doi.org/10.1063/1.4865107.

97. Liu, J., He, X., and Zhang, J.Z.H. (2017). Structure of liquid water – a dynamical mixture of tetrahedral and 'ring-and-chain' like structures. Phys. Chem. Chem. Phys. *19*, 11931–11936. https://doi.org/10.1039/C7CP00667E.

98. Errington, J.R., and Debenedetti, P.G. (2001). Relationship between structural order and the anomalies of liquid water. Nature *409*, 318–321. https://doi.org/10.1038/35053024.

99. Acharya, H., Vembanur, S., Jamadagni, S.N., and Garde, S. (2010). Mapping hydrophobicity at the nanoscale: applications to heterogeneous surfaces and proteins. Faraday Discuss *146*, 353–365. , discussion 367-393, 395-401. https://doi.org/10.1039/B927019A.

100. Kjellander, R. (2019). In Statistical Mechanics of Liquids and Solutions: Intermolecular Forces, Structure and Surface Interactions, 1st ed. (CRC Press). https://doi.org/10.1201/9780429194368.

STAR★METHODS

KEY RESOURCES TABLE

REAGENT or RESOURCE	SOURCE	IDENTIFIER
Software and algorithms		
VASP software	VASP Software GmbH, https://www.vasp.at/	Version 5.4.4
LAMMPS software	Sandia National Laboratory and the US Department of Energy, https://www.lammps.org	29 September 2021 version
Deposited data		
Structures of adsorbates used to compute solvation thermodynamics	https://iochem-bd.bsc.es/browse/	Collection id = 100/254792
Structures of adsorbates used to compute solvation thermodynamics	Ref. [45]	https://github.com/getman-research-group/Depository-Differences-in-solvation-thermodynamics-of-oxygenates-at-Pt-Al2O3-perimeter-versus-Pt-111
Structures of adsorbates used to compute solvation thermodynamics	https://iochem-bd.bsc.es/browse/	https://doi.org/10.19061/iochem-bd-1-37

RESOURCE AVAILABILITY

Lead contact

Further information and requests should be directed to and will be fulfilled by the lead contact, Rachel B. Getman (rgetman@clemson.edu)

Materials availability

This study did not generate new unique materials.

Data and code availability

- Structures of adsorbates used to compute solvation thermodynamics have been deposited at https://iochem-bd.bsc.es/browse/review-collection/100/254792/ff6fe95a2c837891df6fa749 and are publicly available as of the date of publication. The collection id is listed in the key resources table.

- This study did not generate a new code.

- Any additional information required to reanalyze the data reported in this paper is available from the lead contact upon request.

METHOD DETAILS

Pt/Al$_2$O$_3$ simulation supercells

Pt terrace and Pt/Al$_2$O$_3$ perimeter sites are modeled with a platinum (111) slab and a platinum particle supported on an alumina slab, respectively. Pt(111) terrace site models are taken from our prior work[14] and the details are summarized below. Pt/Al$_2$O$_3$ perimeter site models are constructed as follows. Under liquid H$_2$O, Al$_2$O$_3$ can develop a coverage of OH* groups due to H$_2$O dissociation.[35,52] However, as determining the extent of hydroxylation requires calculating the surface free energy and then performing thermodynamic and/or kinetic modeling, evaluation of a hydroxylated surface is reserved for future work. Hence, Pt/Al$_2$O$_3$ models in this work utilize a pristine Al$_2$O$_3$ slab. They are constructed as follows. Al$_2$O$_3$ slabs are built by cleaving a (0001) surface from the structure of bulk α-Al$_2$O$_3$ (space group = R $\overline{3}$ c), which has a calculated lattice parameter of 5.178 Å, in agreement with a previous computational study.[53] Two periodic supercells are employed, one smaller (Figure S1) and computationally efficient for the DFT calculations and a second larger supercell (Figure S2) that more accurately captures interfacial phenomena for the MD simulations. Dimensions of the DFT and MD supercells are a = b = 10.3 Å and c = 32.7 Å and

a = b = 15.5 Å and c = 53 Å, respectively. Supercell angles for both cells are α = β = 90° and γ = 55.3°. Pt nanoparticles are modeled with tetrahedrally shaped Pt_4 particles constructed on the tops of the α-Al_2O_3 slabs, following our prior work.[28] Energies and entropies of solvation calculated using these small Pt_4 particles are compared against analogous values calculated using Pt_8 particles and Pt_{20} and Pt_{48} nanorods below. We find that when the adsorbate geometry and partial charge are held constant, the Pt particle size has a nearly negligible influence on the calculated energies and entropies of solvation (see the model validation sections below); however, when the adsorbate partial charge and geometry are changed, it can influence the calculated entropy of solvation. We find the calculated partial charges have a maximum 0.2 meV/K influence on the calculated entropies of solvation. At 300 K, this results in a 0.07 eV uncertainty in the free energy of solvation, which is within the standard error due to the method[54] as well as the configurational variability caused by thermal disorder in the liquid structure.[55,56] Further, we find that variation of partial charges in the adsorbates is not systematic and hence not due to small particle size effects (see the model validation sections below). Variation of adsorbate geometry is related to the specific adsorption site structure at the Pt/Al_2O_3 interface and hence also not due to small particle size effects. We find that variation in the adsorbate geometry has a maximum 0.4 meV/K influence on the calculated entropies of solvation, which results in a 0.11 eV uncertainty in the free energy of solvation at 300 K, which is also within the uncertainty expected by the MSS method.

Adsorbates are added to the supercells near or on the Pt particles. The closest distances between adsorbates in neighboring periodic images are 8 Å and 13 Å for the DFT and MD supercells, respectively. In prior work we found that lateral interactions between adsorbates at these neighbor distances contribute less than 0.10 eV to the calculated energetics.[28] H_2O molecules are added to the supercells using the MCPliQ code.[39] Specifically, 50 to 60 H_2O molecules are added to the DFT cells, depending on the vacuum volume remaining after the adsorbate is added. The resulting water column heights are 14–15 Å, which guarantee at least three solvation shells.[57] Similarly, 182 to 188 H_2O molecules are added to the MD cells, resulting in water column heights of ∼30 Å. An additional 14 Å of vacuum space is included at the top of the water columns in all supercells.

Solvation free energies

Solvation free energies are calculated using a combination of DFT and MD, following our prior work:[40]

$$\Delta F_{solv}^{MSS} = \Delta E_{int}^{DFT} - T\Delta S_{int}^{MD} \qquad \text{(Equation 1)}$$

where ΔF_{solv}^{MSS} is the Helmholtz free energy of solvation calculated with MSS, ΔE_{int}^{DFT} is the water-adsorbate interaction energy calculated with DFT, and ΔS_{int}^{MD} is the water-adsorbate interaction entropy calculated with MD. A flow diagram illustrating how ΔF_{solv}^{MSS}, ΔE_{int}^{DFT}, and ΔS_{int}^{MD} are calculated is provided in Figure S16. A description of the procedure is as follows. Following construction of the Pt/Al_2O_3 models, adsorbates are added to the supercells and their geometries are optimized in DFT using initial guesses based off those published previously by our group.[28] H_2O molecules are then added to the supercell using the MCPliQ code.[39] Configurations of H_2O molecules are then obtained in the canonical (NVT) ensemble in MD. A tractable number of configurations is then sampled and used to compute ΔE_{int}^{DFT} following our prior work[14,58]:

$$\Delta E_{int}^{DFT} = \left\langle \left(E_{Pt/Al_2O_3 + adsorbate}^{liq} - E_{Pt/Al_2O_3 + adsorbate}^{vac} \right) - \left(E_{Pt/Al_2O_3}^{liq} - E_{Pt/Al_2O_3}^{vac} \right) \right\rangle \qquad \text{(Equation 2)}$$

where $E_{Pt/Al_2O_3 + adsorbate}^{liq}$ is the electronic energy (calculated with DFT) of the Pt/Al_2O_3 model with the adsorbate under liquid water, $E_{Pt/Al_2O_3 + adsorbate}^{vac}$ is the electronic energy of the Pt/Al_2O_3 model with the adsorbate in vacuum, $E_{Pt/Al_2O_3}^{liq}$ is the electronic energy of the Pt/Al_2O_3 model under the same liquid water structure as for $E_{Pt/Al_2O_3 + adsorbate}^{liq}$ but with the adsorbate removed, and $E_{Pt/Al_2O_3}^{vac}$ is the electronic energy of the Pt/Al_2O_3 model without the adsorbate in vacuum.

$T\Delta S_{int}^{MD}$ is calculated from two separate MD simulations, following our previous publications[40,54]:

$$T\Delta S_{int}^{MD} = \Delta E_{int}^{MD} - \Delta F_{sol}^{MD} \qquad \text{(Equation 3)}$$

where ΔE_{int}^{MD} is the average energy of interaction between the H_2O molecules and the adsorbate over an NVT trajectory, and ΔF_{sol}^{MD} is the Helmholtz free energy of solvation of the adsorbate, calculated using the method of free energy perturbation (FEP) in MD. Values used to compute $T\Delta S_{int}^{MD}$ are provided in Table S12.

Values of ΔF_{solv}^{MSS} are compared with the analogous values calculated with implicit solvation in Table S13.

Classical molecular dynamics simulations for Pt/Al$_2$O$_3$ systems

MD simulations are performed with the Large-scale Atomic/Molecular Massively Parallel Simulator (LAMMPS).[59] All MD simulations are carried out at 300 K. In all MD simulations, H$_2$O molecules are allowed to move, while positions of Al$_2$O$_3$, Pt, and adsorbate atoms are held fixed. Following addition of H$_2$O molecules using MCPliQ,[39] an initial geometry relaxation is performed to refine the initial water configuration and then the simulation of interest is carried out.

NVT simulations used to generate H$_2$O molecule configurations

NVT simulations are carried out to obtain configurations of H$_2$O molecules for calculating ΔE_{int}^{DFT}, ΔE_{int}^{MD}, the sizes of the cavities created by the adsorbates, and the average number of hydrogen bonds formed between H$_2$O molecules and the adsorbates. In all these simulations, temperature is maintained with the Nosé–Hoover thermostat,[60,61] a 1 fs timestep is employed, and the first 5 ns of the simulation are used for system equilibration. Production runs and sampling frequencies for the various quantities are as follows. Production runs for generating configurations of H$_2$O molecules used to calculate ΔE_{int}^{DFT} are 3 ns long, and configurations are sampled every 0.3 ns (resulting in a total of 10 configurations). As 0.3 ns is significantly longer than hydrogen bond lifetimes of oxygenate species,[14] this sampling frequency ensures that these 10 configurations are uncorrelated. The ensemble average for ΔE_{int}^{DFT} is then calculated by evaluating Equation 2. Production runs for generating configurations of H$_2$O molecules used to calculate ΔE_{int}^{MD} are 5 ns long, and configurations are sampled every 0.001 ns. The ensemble average is obtained by computing the average energy of interaction between the H$_2$O molecules and the adsorbate. Production runs for generating configurations of H$_2$O molecules for computing adsorbate cavity sizes are 9 ns long, and configurations are sampled every 0.01 ns. The cavity size is approximated as the number of equivalent H$_2$O molecules that are displaced by the adsorbate. Hence, the ensemble average is taken as the average number of water molecules within 12 Å of the surface when the adsorbate is not present (calculated from the density of water in that region) minus the average number of water molecules within 12 Å of the surface when the adsorbate is present. Finally, production runs for generating configurations of H$_2$O molecules used to calculate the average number of hydrogen bonds between H$_2$O molecules and adsorbates are 9 ns long, and configurations are sampled every 0.3 ns. The ensemble average is calculated by averaging the number of H$_2$O molecules that fit geometric criteria for hydrogen bonding,[62] i.e., the $O_{H_2O} - O_{adsorbate}$ distance ≤ 3.5 Å and either the $O_{H_2O} - O_{adsorbate} - H_{adsorbate}$ or $O_{H_2O} - O_{adsorbate} - H_{H_2O}$ angle $\leq 30°$. Using this criterion, both hydrogen bond donors and acceptors are counted.

Force fields and parameters for Pt/Al$_2$O$_3$ systems

Following our prior publication,[40] interactions between H$_2$O molecules and catalyst and adsorbate atoms are calculated using Lennard-Jones plus Coulomb potentials, where the long-range Coulombic interactions are captured using the Particle−Particle Particle−Mesh (PPPM) method.[63] Lennard-Jones parameters for adsorbate atoms are taken from the OPLS-AA[64] force field. Lennard-Jones parameters for Pt atoms are obtained using a modified version of the United Force Field (UFF)[65] (see below). Lennard-Jones parameters for the Al$_2$O$_3$-water interaction are taken from a force field parameterized from DFT data by Ciacchi et al.[66] This force field was shown to produce water structures in agreement with DFT when coupled with the TIP3P water model;[66] hence, Lennard-Jones parameters for H$_2$O molecules are taken from the TIP3P/CHARMM[67] water model. Arithmetic mixing rules are used for H$_2$O-H$_2$O and H$_2$O-Pt interactions, while the remaining interactions employ geometric mixing rules.

It has been shown that calculated enthalpies, entropies, and free energies of hydration are sensitive to the water model that is employed.[68,69] In the MSS method, energies of solvation are computed with DFT. Hence, the water model is more likely to influence entropies of solvation. Entropies of hydration computed using the TIP3P/CHARMM model are compared with values computed using the SPC/E model[70] in Table S6. We find that the choice of water model gives a maximum 0.2 meV/K difference in the calculated entropies of hydration. At 300 K, this results in a 0.05 eV uncertainty in the free energy of hydration. Further, we previously showed that free energies of solvation for constituents of sugar alcohols and ammonia on Pt(111) calculated using the MSS method where the MD simulations employed the TIP3P/CHARMM water model were in excellent agreement with free energies of solvation calculated with implicit solvation for adsorbates that do not form strong hydrogen bonds with H$_2$O (i.e., which can be appropriately modeled with implicit solvation[40]). These results suggest that the water model has a minor influence on the calculated solvation thermodynamics for the species studied herein; however, the influence likely becomes more dramatic as the hydration energy becomes stronger.

Coulomb charges on the atoms in the H_2O molecules are taken from the TIP3P/CHARMM force field. Coulomb charges on the atoms in Al_2O_3 are taken from the force field by Ciacchi et al.,[66] with slight modifications made to account for charge transfer due to binding with the Pt particle (see below). Coulomb charges for adsorbate and Pt atoms are the partial charges calculated from DFT using the DDEC6 atomic population analysis method,[71] with minor modifications. All Lennard-Jones and Coulomb parameters are listed in Tables S7 and S10.

Free energy perturbation calculations

ΔF_{sol}^{MD} are calculated using the methods of FEP and thermodynamic integration, following ref.[72–75] and our prior work.[40] In these methods, a solute is "grown" in a solvent over the course of a NVT simulation by gradually "turning on" the interaction between solvent and solute. A thermodynamic integration is performed on the energy of the system to compute ΔF_{sol}^{MD}. In this work, the general strategy is that the solute is the adsorbate, and the solvent is H_2O. During the FEP simulations, Leonard-Jones parameters and Coulomb charges are scaled (with coupling parameter λ) for the adsorbate. The Pt particle and Al_2O_3 slab are not scaled. Rationale for this modeling choice is discussed below. Scaling is performed in 50 steps, following the suggestion of Chipot.[74] For each step, an NVT simulation is performed for 300 ps, which yields a total simulation time of 15 ns (including separate scaling of the Lennard-Jones and Coulomb contributions to the energy[74]).

DFT calculations

DFT calculations are performed using the Vienna Ab initio Simulation Package (VASP)[76–80] using PAW 2002 pseudopotentials,[81,82] the PBE exchange correlation functional,[83,84] and D3 dispersion corrections with Becke-Johnson damping.[85,86] Plane waves are included to an energy cutoff of 400 eV, spin polarization is turned on, and dipole corrections are applied in the direction normal to the surface. The first Brillouin zones are sampled using 7 × 7 × 1 Monkhorst–Pack Gamma-centered k-point meshes.[87] Electronic energies are calculated self-consistently and considered to be converged when the difference between subsequent iterations falls below 10^{-6} eV. In geometry relaxations performed in vacuum, all atoms in the supercell are allowed to relax. In geometry relaxations performed in water, the adsorbate is allowed to relax, while all other atoms are held fixed. Geometries are considered converged when the forces on all atoms allowed to relax fall below 0.03 eV/Å.

Model validation: Simulation supercells for the perimeter sites

Pictures of the different simulation supercells that were used for the main results and testing are shown in Supporting Information. Figure S1 for DFT results in the main text. Figure S2 for MD results in the main text. Figures S3–S5 for validation.

Model validation: Density profiles for the perimeter sites

The choice of supercell model for the DFT and MD simulations was made in based on a molecular density analysis, obtained by plotting the molecular density versus distance from the surface. The water-alumina interface presents a double layer phenomenon due to the hydrophilicity of the alumina.[33] The double layer effect is reflected graphically as two marked peaks represented a higher local density near the surface. This layering phenomenon emerges in different scenarios, for example in the electric double layer[47] and near hydrophilic surfaces[88] where a strong interaction is found between the surface and the solvent (this is lost as we move away from the surface); causing a higher local density near the surface compared with the bulk conditions. The density profile of the water alumina interface, including the presence of the supported platinum cluster/particle, in three different supercell is shown in Figures S6–S8. The final MD supercell (Figure S8) was chosen for the main text because it most properly captures the layering phenomena. This third model (Figure S8) which correspond to the 3 × 3 × 2 unit cell was selected because it more accurately describes the double layer effect in the alumina-water interface as previously described by Striolo[33] and obtains smoother ensemble averages for water properties (as a larger number of water molecules is employed), for instance compared to the smoothness of bulk water conditions in the three simulations cells. The first layer peak for this model is reach around ~9.1 Å of box height with a global maximum density of ~2.1 g/cm^3, the second layer is reach with a second peak around ~10.6 Å of box height with a relative maximum around ~1.3 g/cm^3.

The simulation supercells are built from the original alumina bulk unit cell 1 × 1 × 1 with lattice parameter of 5.178 Å, the expanded versions are multiples of this cell, for example the 2 × 2 × 2 unit supercell contains double the number of atoms from the original supercell in each dimension. Liquid water is added to all of these supercells in the vacuum regions shown in Figures S1–S5, and a vacuum space of ≥14 Å is added above the tops of the water columns in all models used in this work. The rationale to add vacuum space is that when no vacuum space is added, bulk water density cannot be reached, as shown in Figure S6. Figure S7 correspond to the 2 × 2 × 2 units cell with ~14 Å of additional vacuum added, the reason to employ the vacuum is to get the correct bulk water density; because the alumina surface disturbs the water structure around ~8 Å above the surface and because the periodic boundary conditions will require a larger number of water molecules to reach bulk water density.

Pt(111) simulation supercells

Two simulation supercells were used to model Pt(111) systems: one small and efficient cell for the interaction energies from DFT and solvation entropy in the results section (Figure S9) and a larger simulation supercell for the discussion section (Figure S10). All other simulation details follow our previous works.[14,39,40,55,58] The data presented in the results section from the Pt(111) system used a Platinum (111) supercell with the following dimensions as in our previous work:[14] a = b = 8.4 Å and c = 24 Å with the angles $\alpha = \beta = 90°$ and $\gamma = 60°$. H_2O molecules are added to the supercell using the MCPliQ code.[39] In this simulation supercell vacuum was not used for the MD simulations (i.e., the entire vacuum region was filled with H_2O) and for DFT calculations an additional 14 Å of vacuum was added at the top of the water column, following our prior works.[14,39,55] A larger Platinum (111) slab model was used for data presented in the discussion section that allowed a better computation of ensemble average properties in the adsorbates involved in methanol dehydrogenation, this supercell has the following dimensions a = b = 16.8 Å and c = 53 Å. This supercell has the angles $\alpha = \beta = 90°$ and $\gamma = 60°$ and is shown in Figure S10.

Classic molecular dynamics simulations for Pt(111) systems

MD simulations are performed following the methodology from our prior publications.[14] An initial geometry relaxation was performed to refine the initial water configuration. Then, a 0.5 ns simulation in the NVE ensemble is carried out to equilibrate the initial water configuration to the production temperature (300 K), followed by 5 ns in NPT ensemble to adjust the simulation cell height and obtain the appropriate water density, then 2 ns of final equilibration in a NVT ensemble. The production run in is carried out in the NVT ensemble for 5 ns.

List of adsorbates included used for solvation thermodynamic trend for terrace sites

The list of 90 adsorbates used in the results Section were obtained from previous works from our group[14] and the structures of decomposition steps of C_1–C_2 alcohols from Lopez.[89] The structures are available in Getman Research Group GitHub.[90] This list include different oxygenates from C_1-C_3 organic molecules with different functional groups, among them alcohols, polyols, ketones, diketones and non-oxygenated intermediates.

Model validation: Effect of calculated partial charges on solvation entropy for the Pt/Al$_2$O$_3$ systems

The solvation entropy was calculated according to Equation 3 in the main text using different perimeter site models. To evaluate the influence of the adsorbate charges, which are affected in some extent by the charge transfer to the Platinum cluster, we calculated partial charges and solvation entropies using different Pt cluster sizes. A summary of partial charges on Pt_4, Pt_8, and Pt_{20} models is provided in Table S1. From this table, the adsorbate partial charge does not vary in a systematic way for all adsorbates with Pt cluster size. For example, the partial charge of CH_2OH gets more positive as the Pt cluster size increases, while the partial charge for COH gets more negative at the small Pt_4 and gets diluted at larger particle sizes, and the partial charge for CHOH is nearly constant across all three cluster sizes. Given that there will be a distribution of cluster sizes in a real supported catalyst, this means that no one cluster size model is more correct or more incorrect than any other when it comes to computing partial charges.

Table S2 shows a comparison for solvation entropies calculated using the Pt_4/Al_2O_3 and Pt_8/Al_2O_3 models. The observed differences are in average 0.08 eV which is comparable with DFT differences. These comparisons also take into account some geometrical differences; an example of the differences for CH_2OH are

shown in Figure S11. Considering that some differences could emerged due to the adsorbate and Platinum particle geometry (for example, compare entropies for CHOH on Pt_4 vs. Pt_8, where the charges are nearly identical), this comparison shows that charges derived from the Pt_4 cluster model can capture adequately the solvation entropy.

Model validation: Testing of the platinum particle size on the solvation entropy for the Pt/Al₂O₃ systems

To test the impact of the Pt particle model size on the calculated solvation entropy, an extended version of the MD simulation supercell with dimensions a = 25.88 Å, b = 15.5 Å, c = 53 Å, and α = β = 90°, and γ = 55.3° and a larger Pt_{48} nanorod model was created (see Figure S5). This model is computationally intractable for DFT calculations; hence it was only tested in the MD simulation. To isolate the influence of the cluster size; the same adsorbate geometry and net adsorbate and cluster charges from the adsorbate and Pt_4 cluster model were used in the larger Pt_{48} nanorod model. Comparisons of the entropy of solvation of CH₂OH* are made in Table S3. CH₂OH was chosen as a model adsorbate because it does not present a large charge transfer and forms bonds with both alumina and Pt. As can be seen, the size of the Pt particle model has only a minor difference on the calculated entropy of solvation and hence the entropies of solvation reported in the manuscript are calculated using the more efficient Pt_4 cluster model.

Model validation: Testing of the platinum particle size for interaction energy with DFT

To test the impact of the cluster size in the interaction energy with DFT, a larger Pt_{20} nanorod model (Figure S4) in a wider supercell was tested and compared with the Pt_4 model. In this wider simulation supercell, the Platinum cluster and alumina slab was kept fixed, and the adsorbate was allowed to relax. In Table S4 is shown that the Platinum cluster size has a minor influence on the Interaction energy with DFT and hence interaction energies reported in the manuscript are calculated using the Pt_4 clusters.

Model validation: Testing for the solvation thermodynamics for the slab size in the terrace site Pt(111) model

In the results section a comparison of the solvation thermodynamic in the terrace and perimeter sites was provided. The results presented in that section from the terrace sites was obtained from the Pt(111) slab model according to Figure S9 (8.4 Å of lateral size), this is a small and efficient model that allowed a high throughput calculation and to test the influence of the slab size on the solvation thermodynamics with this small model a comparison with the larger slab model presented in Figure S10. The comparison shown in Table S5 reflects similar free energy values, in the case of ΔE_{int}^{DFT} (eV) the difference is within the uncertainty of ± 0.10 eV as in our prior publications.[54] For this reason, this small cell is considered sufficient to capture the trend between $T\Delta S_{int}^{MD}$ and ΔE_{int}^{DFT}; and the trend for the larger number of Pt(111) adsorbates was made with this DFT efficient smaller cell. Hence, the small cell was used to obtain the enthalpy and entropy results presented in the main text, and the large cell was used to explain the trends in the discussion section.

Model validation: Selection of the water model

Regarding the selection of water model to capture the water behavior; different water models have been proposed with different errors depending on the desired property. In the case of solvation free energies models like TIP3P, SPC, TIP4P are widely used, and their performances are mostly similar.[68] An exception of this is the case of amino acids with the TIP3P model, which is outperformed by the TIP4P model.[69] But in the case of smaller molecules, like the alcohols in our case of study, TIP3P can give better agreement with the experiments than TIP4P and similar performance than SPC/E.[68,91] A comparison of the energies and entropies of solvation calculated with MD using two different water models is provided in Table S6. Since in our multiscale sampling strategy, energies of solvation are computed with DFT, the comparison of the entropies of solvation is most important. We find that the choice of water model has a maximum 0.2 meV/K influence on the calculated entropies of solvation, resulting in a maximum difference of 0.05 eV in the calculated free energies. This difference is within the accuracy of the MSS method itself.

Lennard-Jones and Coulomb parameters used in the MD simulations for Pt/Al₂O₃ systems

Table S7 gives the Lennard-Jones parameters used in the MD simulations in this work. Their rationale is explained in the following sections. A variation of the Universal Force Field (UFF) in the case of Platinum was employed. Additionally, the TIP3P model used the following constants for a flexible water

molecule[59,92]: K of OH bond 450 (kcal/mol), r_0 of OH bond = 0.9572 (Å), K of HOH angle = 55 (kcal/mol) and θ of HOH angle = 104.52°.

Rationale for modifying the Lennard-Jones epsilon parameter for Pt atoms in the Pt/Al₂O₃ systems

Anchoring the Pt particle to the alumina support causes the Pt particle to become negatively charged. Further, addition of some adsorbates causes this charge to become even more negative, in some cases, see Figures S13 and S14 and Table S10. The large negative charges in the Platinum atoms become problematic from a modeling perspective, because the UFF for Platinum was not designed for metallic atoms. The UFF epsilon parameter has a value of 0.0800 kcal/mol, which is relatively small and not large enough to capture a correct Platinum-Water distances; this results in Platinum-Water distances that are sometimes unphysically short, compared with the uncharged metal slab and DFT predicted distances (see Table S8). Figure S12 plots the distribution of the Platinum to Water distances in differences in the first solvation shell, showing that in some cases short Platinum to Water distances are found. For instance, the case of COH*, which is an extreme case has a significantly lower distances, compared with the original UFF epsilon parameter, with an average Platinum-Hydrogen of water distance of 2.18 Å compared with the DFT value of 2.51 Å, and in some configurations with distances less than 1.5 Å, the modified epsilon parameter generates configurations of water with an average distance of 2.49 Å, much closer to the DFT predicted distances. Moreover, when compared the water density profile with the UFF and the Interface Force Field for FCC metals,[93] the latter utilizes a much larger epsilon parameter. Hence, we modified the UFF epsilon parameter for Pt.

Development of Coulomb charges for MD simulations from DFT calculated partial charges for the Pt/Al₂O₃ systems

The Platinum cluster interacts with the alumina surface, causing a charge transfer.[94] Specifically, the Pt₄ cluster takes on a charge of −0.393 (i.e., it receives 0.393 electrons from the Al₂O₃ slab) after binding with the Al₂O₃ slab. Additional charge transfer occurs after the adsorbate is added. Partial charges are calculated using the DDEC6 atomic population analysis method[71] using DFT-calculated charge density. The net charges for the Pt₄ cluster, adsorbate, and Al₂O₃ slab are presented in Figures S13 and S14.

As can be seen in Figures S13 and S14, the addition of the adsorbate can have a large effect on the partial charge on the Pt₄ cluster but only a minor influence on the charge of the Al₂O₃ slab. Hence, the decision was made to keep the Al₂O₃ slab charge constant for every adsorbate and vary the Pt₄ and adsorbate charges. This decision will allow us to simplify the scaling in the free energy calculation, since we are interested in the contribution from the adsorbate and not the alumina slab. The Al₂O₃ net charge that we employed was +0.393, which is the charge of the slab with the Pt₄ cluster but without an adsorbate (see Table S10). To accomplish this, the charge of +0.393 was evenly distributed over all Al and O atoms in the slab. This required making the force field charge of each Al and O atom in the slab more positive by ~0.005 in the DFT cell and ~0.0022 in the MD cell, which is minor enough to not influence MD results. The charges used for Al and O atoms in the Al₂O₃ slab in the MD simulations are given in Table S9 and compared with the original charges recommended in the force field by Ciacchi.[66]

Adsorbate and Pt₄ cluster charges were then constructed as follows. After the addition of the adsorbate if a net charge of the cluster and adsorbate differ from the alumina charge, the difference was evenly distributed over the Pt cluster and adsorbate atoms. For example, for CH₃OH* the alumina net charge is +0.405, the clean supported Platinum cluster is +0.393, this implies a change of +0.012. This charge of +0.012 was then distributed in all adsorbate and Platinum cluster atoms. In this example, the charge of each adsorbate and Pt cluster atom was made more positive by 0.0012 (0.0012 = 0.012/10, where 10 is the number of atoms in CH₃OH + Pt₄). Table S10 gives all calculated partial charges as well as modified charges that were used in the MD simulations for all adsorbates considered in this work.

Reflective wall in MD simulations for Pt/Al₂O₃ systems

To prevent that in a rare occasion one water molecule escapes the water column (water to vacuum interface in Figures S7 and S8) and travel to the bottom part of the alumina slab due to the periodic boundary conditions, a Leonard Jones wall located 14 Å below the top of the simulation box was included in all MD simulations. Any water molecule that escapes the water to vacuum interface, will eventually hit the wall and will

be reflected again to the water column. An analogously scheme was used by Hess to prevent water molecules to escape from a region.[95]

Justification of scaling strategy used for the FEP simulations of the Pt/Al$_2$O$_3$ systems

On one hand, we acknowledge that the charge redistribution of the Platinum particle is a real contributor for the solvation free energy, but on the other hand this is very minor for most of the adsorbates in the Pt$_4$ cluster model (see for a comparison of the two scaling schemes in Table S11). The two exceptions found (COH and CHOH) correspond to a small cluster effect, that caused high Platinum charges, that are not accurately described by the force field and get diluted at larger Platinum particle sizes (see above). This is because the large partial charges induce an artificially large Platinum-Water interaction that would not be realized on larger Pt particles. For all other adsorbates, the size of the Pt particle does not have a significant influence on the calculated free energies. For this reason, we limited the scaling scheme to the adsorbates and keeping the small and computationally tractable Pt$_4$ cluster model for DFT calculations. The Al$_2$O$_3$ slab is present during the FEP simulations, but it is not included in the scaling for two reasons: 1) the alumina charges are held fixed for all adsorbates, as it is mostly unaffected by the adsorbate, 2) some of the adsorbates in the catalytic sites cover some surface area in the alumina, not scaling the alumina will avoid to capture this undesired contribution; as the replacement of a hydrated site with the adsorbate (or vice versa) can have a significant influence the reaction thermodynamics and will be treated with an explicit water molecule in a future research.

A summary of partial charges of the Pt$_4$, Pt$_8$, and Pt$_{20}$ cluster models on a per Pt atom basis is provided in Figure S15. The results show that the charge per Pt decreases as the cluster size gets larger, to the extent of being diluted as the particle sizes increase. Hence, while particle size does not influence adsorbate partial charge in a systematic way, it does influence Pt cluster size in a systematic way. For this reason, and also since we wish to restrict the calculation of solvation thermodynamics to the adsorbates themselves (and not the Pt cluster) the scaling in the free energy calculation does not include the platinum particle.

On our previous studies,[40,54] in the calculation of the solvation free energy and entropy with MD, the Platinum atoms were included in the scaling of the FEP calculation, accounting for the Coulombic component in the solvation, due to charge redistribution in the Platinum atoms. A comparison of the solvation entropy calculated with the previous studies[40,54] scheme, including both the adsorbate and the Platinum Coulombic component (Scaling: Ads(LJ + Coul)+Pt(Coul)) and the method employed in the main text, only scaling the adsorbate (Scaling: Ads(LJ + Coul)) is provided in Table S11. The inclusion of this component in most of the cases had a minor effect in the solvation entropy, with the exception of COH and CHOH, because they presented high cluster charges; the charge transfer effect is diluted with larger Platinum particles. This justifies not including the Platinum in the scaling, to avoid any small cluster effect in the cases of COH and CHOH, keeping the same scaling scheme in all adsorbates and still capturing the relevant interaction in the solvation entropy.

Comparison of free energy between the multiscale sampling method and implicit solvation

A comparison was made with the solvation free energy calculated with the multiscale sampling model reported in the results section with VASP implicit solvation method published by Mathew et al.[96] The comparison is shown in Table S13.

Order parameters for water structure

Molecular structure of water has been previously studied on the literature,[41] the water structure resembles, even though not perfectly, a tetrahedral or a "ring-and-chain" like structure for liquid water.[97] Two classical features based on the work of Debenedetti et al.[98] that measure the degree organization of water are based on the radial distribution of water and the degree of matching a tetrahedral structure are: the orientational order parameter (q) which measures the angle organization degree of hydrogen bonding and the translational order parameter (t), related to the oxygen water distance distribution homogeneity; when these parameters approached to zero the water structure resembles the ideal gas configuration and higher number means a more ice like structure. To characterize and compare the structure of interfacial water, these two organizational features were estimated for the different structures in the alumina base system and pure aqueous conditions of water formaldehyde and methanol. The order parameters for the list of adsorbates, adding the pure water, a formaldehyde molecule and a methanol molecule in the bulk aqueous conditions are shown in Figure S21. The results show that the alumina-based system has a higher

translational order parameter and a lower orientational order parameter. The increase in the translational order in the alumina-based system is related to the higher packing increase of the interfacial water and the decrease in the orientational order parameter is attributed to the reorganization of water towards the alumina surface, breaking the bulk hydrogen bonding structure of water.

Isothermal compressibility of water

The thermal fluctuation of the solvent is a property of the liquid that can be related to the solvation thermodynamics, as a solvent that presents more fluctuation can more easily accommodate a solute,[36,99] as it is also more mobile. The isothermal compressibility factor for the first layer of the Pt(111) and Alumina based systems was calculated following Kjellander[100] and normalizing it to the respective volume of water in the bulk solutions, a value of 1 indicates the same compressibility of water in bulk conditions and a lower values means a lower compressibility compared with bulk water conditions, see Equation 4. The results are shown in Table S15. The behavior of the Alumina system shows a lower compressibility than the Platinum systems, this is related to the magnitude of the entropic penalty that will be required to accommodate the adsorbate in both systems, being the alumina more penalized in this aspect.

$$\text{Relative isothermal compressibility of water } = \frac{\left.\frac{\langle N^2 \rangle - \langle N \rangle^2}{\langle N \rangle}\right|_{Surface}}{\left.\frac{\langle N^2 \rangle - \langle N \rangle^2}{\langle N \rangle}\right|_{Bulk}} \qquad \text{(Equation 4)}$$

Effect of the sample size in the coefficient of determination for the entropy and interaction energies in Pt(111)

To evaluate the effect of the sample size on the coefficient of determination (R^2) in the Pt(111) results section (Figure 4) a bootstrap simulation was performed with a sample size of 10, equal to the number of adsorbates for the Pt/Al$_2$O$_3$ system. The distribution of bootstrapped sample is shown in Figure S22. The percentile confidence interval at 95% of the R^2 for the Pt(111) data was [0.79, 0.98], this implies that the smaller sample size of the Pt/Al$_2$O$_3$ cannot by itself explain the decrease in the R^2 from the Pt(111) system (0.91) to the Pt/Al$_2$O$_3$ system (0.62), indicating that some intrinsic differences between terrace and perimeter sites occurs, with an impact in the solvation thermodynamic correlation behavior presented herein.